



HAL
open science

Three-axial shape distributions of pebbles, cobbles and boulders smaller than a few meters on asteroid Ryugu

Tatsuhiro Michikami, Axel Hagermann, Tomokatsu Morota, Yasuhiro Yokota, Seitaro Urakawa, Hiroyuki Okamura, Naoya Tanabe, Koki Yumoto, Tatsuki Ebihara, Yuichiro Cho, et al.

► To cite this version:

Tatsuhiro Michikami, Axel Hagermann, Tomokatsu Morota, Yasuhiro Yokota, Seitaro Urakawa, et al.. Three-axial shape distributions of pebbles, cobbles and boulders smaller than a few meters on asteroid Ryugu. *Icarus*, 2022, 381, pp.115007. 10.1016/j.icarus.2022.115007 . hal-03674912

HAL Id: hal-03674912

<https://u-paris.hal.science/hal-03674912>

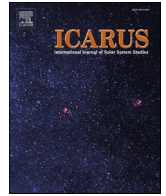
Submitted on 21 May 2022

HAL is a multi-disciplinary open access archive for the deposit and dissemination of scientific research documents, whether they are published or not. The documents may come from teaching and research institutions in France or abroad, or from public or private research centers.

L'archive ouverte pluridisciplinaire **HAL**, est destinée au dépôt et à la diffusion de documents scientifiques de niveau recherche, publiés ou non, émanant des établissements d'enseignement et de recherche français ou étrangers, des laboratoires publics ou privés.



Distributed under a Creative Commons Attribution - NonCommercial - NoDerivatives 4.0 International License



Three-axial shape distributions of pebbles, cobbles and boulders smaller than a few meters on asteroid Ryugu

Tatsuhiro Michikami^{a,*}, Axel Hagermann^b, Tomokatsu Morota^c, Yasuhiro Yokota^d, Seitaro Urakawa^e, Hiroyuki Okamura^f, Naoya Tanabe^g, Koki Yumoto^c, Tatsuki Ebihara^c, Yuichiro Cho^c, Carolyn M. Ernst^h, Masahiko Hayakawa^d, Masatoshi Hirabayashiⁱ, Naru Hirata^j, Chikatashi Honda^j, Rie Honda^k, Shingo Kameda^l, Masanori Kanamaru^d, Hiroshi Kikuchi^d, Shota Kikuchi^m, Toru Kouyamaⁿ, Moe Matsuoka^o, Hideaki Miyamoto^p, Takaaki Noguchi^q, Rina Noguchi^{r,d}, Kazunori Ogawa^d, Tatsuaki Okada^d, Naoya Sakatani^l, Sho Sasaki^s, Hirotaka Sawada^d, Chiho Sugimoto^c, Hidehiko Suzuki^t, Satoshi Tanaka^d, Eri Tatsumi^{u,c}, Akira Tsuchiyama^{v,w,x}, Yuichi Tsuda^d, Sei-ichiro Watanabe^f, Manabu Yamada^m, Makoto Yoshikawa^d, Kazuo Yoshioka^y, Seiji Sugita^{c,m,y,z}

^a Faculty of Engineering, Kindai University, Hiroshima Campus, 1 Takaya Umenobe, Higashi-Hiroshima, Hiroshima 739-2116, Japan

^b Luleå University of Technology, Space Campus, 981 28 Kiruna, Sweden

^c Department of Earth and Planetary Science, Graduate School of Science, The University of Tokyo, 7-3-1 Hongo, Bunkyo-ku, Tokyo 113-0033, Japan

^d Institute of Space and Astronautical Science (ISAS), Japan Aerospace Exploration Agency (JAXA), 3-1-1 Yoshinodai, Chuo-ku, Sagami-hara 252-5210, Japan

^e Japan Spaceguard Association, Bisei Spaceguard Center 1716-3 Okura, Bisei, Ibara, Okayama 714-1411, Japan

^f Graduate School of Environmental Studies, Nagoya University, Furo-cho, Chikusa-ku, Nagoya 464-8601, Japan

^g Japan Aerospace Exploration Agency (JAXA), 7-44-1 Jindaiji Higashi-machi, Chofu-shi, Tokyo 182-8522, Japan

^h The Johns Hopkins University Applied Physics Laboratory, Laurel, MD 20723, United States

ⁱ Department of Aerospace Engineering, Department of Geosciences, Auburn University, 211 Davis, Auburn, AL 36849, United States

^j Graduate School of Computer Science and Engineering, University of Aizu, Tsuruga, Ikkimachi, Aizu Wakamatsu, Fukushima 965-8580, Japan

^k Department of Information Science, Kochi University, 2-5-1 Akebono-cho, Kochi, 780-8520, Japan

^l Department of Physics, Rikkyo University, 3-34-1 Nishi-Ikebukuro, Toshima-ku, Tokyo 171-8501, Japan

^m Planetary Exploration Research Center, Chiba Institute of Technology, 2-17-1 Tsudanuma, Narashino 275-0016, Japan

ⁿ Digital Architecture Research Center, National Institute of Advanced Industrial Science and Technology, 2-3-26, Aomi, Koto-ku, Tokyo 135-0064, Japan

^o Laboratoire d'Etudes Spatiales et d'Instrumentation en Astrophysique, Observatoire de Paris, 5 place Jules Janssen, 92195 Meudon, France

^p Department of Systems Innovation, The University of Tokyo, 7-3-1 Hongo, Bunkyo-ku, Tokyo 113-8656, Japan

^q Division of Earth and Planetary Sciences, Graduate School of Science, Kyoto University, Kitashirakawa-iwake-cho, Sakyo-ku, Kyoto 606-8502, Japan

^r Faculty of Science, Niigata University, 8050 Ikarashi 2-no-cho, Nishi-ku, Niigata 950-2181, Japan

^s Department of Earth and Space Science, Osaka University, 1-1 Machikaneyama-cho, Toyonaka 560-0043, Japan

^t Department of Physics, Meiji University, Kawasaki, 1-1-1 Higashimita, Tama-ku, Kawasaki 214-8571, Japan

^u Instituto de Astrofísica de Canarias, Calle Vía Láctea, s/n, 38205 San Cristóbal de La Laguna, Santa Cruz de Tenerife, Spain

^v Research Organization of Science and Technology, Ritsumeikan University, 1-1-1 Nojihigashi, Kusatsu, Shiga 525-8577, Japan

^w CAS Key Laboratory of Mineralogy and Metallogeny/Guangdong Provincial Key Laboratory of Mineral Physics and Materials, Guangzhou Institute of Geochemistry, Chinese Academy of Sciences (CAS), 511 Kehua Street, Wushan, Tianhe District, Guangzhou 510640, China

^x CAS Center for Excellence in Deep Earth Science, Guangzhou 510640, China

^y Department of Complexity Science and Engineering, The University of Tokyo, 5-1-5 Kashiwanoha, Kashiwa, Chiba 277-8581, Japan

^z Research Center for the Early Universe, The University of Tokyo, 7-3-1 Hongo, Bunkyo-ku, Tokyo 113-0033, Japan

* Corresponding author.

E-mail address: michikami@hiro.kindai.ac.jp (T. Michikami).

ARTICLE INFO

Keywords:

Asteroids
Surfaces
Impact process
Asteroid Ryugu
Regolith

ABSTRACT

Over a broad size range, the shapes of impact fragments from catastrophic disruptions are distributed around the mean axial ratio 2: $\sqrt{2}$: 1, irrespective of experimental conditions and target materials. Although most blocks on asteroids are likely to be impact fragments, there is not enough quantitative data for reliable statistics on their three-axial lengths and/or ratios because it is difficult to precisely estimate the heights of the blocks. In this study, we evaluate the heights of blocks on asteroid Ryugu by measuring their shadows. The three-axial ratios of ~ 4100 small blocks with diameters from 5.0 cm to 7.6 m in Ryugu's equatorial region are investigated using eight close-up images of narrower localities taken at altitudes below 500 m, i.e. at < 5.4 cm/pixel resolution, obtained immediately before the second touch-down of the Hayabusa2 spacecraft. The purpose of this study is to investigate the block shape distribution, which is important for understanding the geological history of asteroid Ryugu. Specifically, the shape distribution is compared to laboratory impact fragments. Our observations indicate that the shape distributions of blocks smaller than 1 m on Ryugu are consistent with laboratory impact fragment shape distributions, implying that the dominant shape-determining process for blocks on Ryugu was impact fragmentation. Blocks several meters in size in the equatorial region seem to be slightly flatter than the rest, suggesting that some blocks are partly buried in a bed of regolith. In conclusion, the shape distributions of blocks from several-cm to several-m in the equatorial region of asteroid Ryugu suggest that these are mainly fragments originating from the catastrophic disruption of their parent body and/or from a later impact.

1. Introduction

In laboratory impact experiments, the shapes of fragments from catastrophic disruptions defined by their axes a , b and c , have been found to behave in a very regular way. $a \geq b \geq c$ are the maximum dimensions of the fragments in three mutually orthogonal planes. In catastrophic disruption, the axial ratios of fragments are distributed around mean values of $b/a \sim 0.7$ and $c/a \sim 0.5$, i.e. corresponding to $a:b:c$ in the simple proportion 2: $\sqrt{2}$: 1 (Fujiwara et al., 1978; Capaccioni et al., 1984, 1986; Durda et al., 2015; Michikami et al., 2016, 2018). This regularity of shapes can be observed for a wide range of impact conditions and target materials. It is observed over a size range from particles returned from asteroid Itokawa ($\sim 100 \mu\text{m}$) to small monolithic asteroids (~ 100 m) (Table 1).

Michikami et al. (2010) and Michikami and Hagermann (2021), who investigated the axial ratio b/a of boulders on Eros, Itokawa and Ryugu, propose that the actual shape distribution of the boulders on any asteroid is similar to laboratory impact fragments. Their hypothesis is underpinned by the following three findings (Michikami et al., 2019).

- (i) In laboratory impact experiments, fragment shapes from catastrophic disruptions have been found to behave similarly, independent of experimental conditions and target materials. This result turns out to be valid for fragments ranging from several tens of microns to several cm (Michikami et al., 2016, 2018).

- (ii) Although only limited data on boulders whose three-axial lengths have been measured are available, the mean b/a and c/a ratios of boulders on Itokawa (Michikami et al., 2016) and Ryugu (Michikami et al., 2019) are similar to laboratory impact fragments. The sizes of these boulders, considered to be impact fragments of the parent body, range from several meters to several tens of meters.
- (iii) The mean b/a ratios of small- and fast-rotating asteroids, i.e. those with a diameter < 200 m and a rotation period < 1 h considered to be monolith bodies, are similar to laboratory impact fragments (Michikami et al., 2010).

These three findings strongly suggest that the shapes of fragments from catastrophic disruptions are size-independent. However, there has been no research on three-axial lengths of small blocks on asteroids in previous studies, as it is difficult to quantitatively estimate the height of the boulders on asteroid surfaces. By small blocks in this context, we mean rocks smaller than a few meters, i.e. small boulders, cobbles and pebbles. The close-up images of asteroid Ryugu's surface taken by the Hayabusa2 spacecraft are suitable for measuring three-axial lengths of small blocks because of Ryugu's simple shape and spin axis; since Ryugu is a top-shaped asteroid with a spin axis almost perpendicular to the ecliptic plane, shadows are always horizontal (i.e. east-west direction) in the images (Watanabe et al., 2019; Sugita et al., 2019). Thus, in order to test our hypothesis, we have measured the three-axial lengths a , b and c of blocks smaller than a few meters on the surface of Ryugu based on the close-up images.

Table 1

Shapes of fragments of various sizes and materials.

	Size [m]	Mean b/a ratio	Mean c/a ratio	
Laboratory impact fragments [basalt] (46–120 μm , 241 fragments)	$< 10^{-4}$	0.71	0.50	Michikami et al. (2018) (shot s2126,S)
Laboratory impact fragments [L5 chondrite] (46–120 μm , 292 fragments)	$< 10^{-4}$	0.71	0.52	Michikami et al. (2018) (shot s3105,S)
Itokawa regolith particles (14–114 μm , 47 particles)	$< 10^{-4}$	0.72	0.44	Tsuchiya et al. (2014)
Laboratory impact fragments [basalt] (4–34 mm, 541 fragments)	10^{-3} – 10^{-2}	0.73	0.47	Michikami et al. (2016)(shot s2127)
Small blocks [Ryugu] (5.0 cm –7.6 m, ~ 4100 fragments)	10^{-1} –1	–	–	This study
Large Boulders [Itokawa] (8–40 m, 21 boulders)	10	0.66	0.46	Michikami et al. (2016)
Large Boulders [Ryugu] (6–140 m, 121 boulders)	10 – 10^2	0.71	0.44	Michikami et al. (2019)
Small monolithic asteroids (diameter < 200 m and rotation period < 1 h, 42 asteroids)	10^2	0.71	–	Michikami et al. (2010)

It is also important to estimate apparent three-axial lengths of small blocks for ensuring the safe touchdown of a spacecraft on an asteroid surface. For instance, in the case of Hayabusa2 and OSIRIS-REx, the two most recent missions to conduct touch-and-go surface encounters on small asteroids Ryugu and Bennu, landing site selection was complicated by the abundance of numerous boulders on their surfaces (Kikuchi et al., 2020; Lauretta et al., 2019; Walsh et al., 2019). As these spacecraft are several meters in size, a safe touchdown required accurate knowledge of the three-dimensional shapes of blocks a few m in size and smaller. Therefore, boulder shapes near the touch-down sites were estimated on these missions, but little is known on the statistical three-axial shape distribution of these small blocks on a global scale. In this study, we have measured the three-axial ratios of several thousand small blocks on Ryugu and examined these block shapes for statistical trends.

2. Methodology

In this paper, we define a block as an isolated positive relief feature and we largely follow Wentworth's (1922) classification into pebbles (4–64 mm), cobbles (64–256 mm) and small boulders (> 256 mm). Isolated positive relief features might include partially buried blocks, weathered blocks with subdued outlines, piles of regolithic scree, protruding bedrocks, raised crater rims, and intersecting crater walls. In order to obtain the shape distribution of small blocks on the surface of Ryugu, we analyze several Optical Navigation Camera (ONC) close-up images taken by the Hayabusa2 spacecraft at altitudes below 500 m, i. e. at <5.4 cm/pixel resolution. The width of the close-up images taken at an altitude of 500 m is about 55 m, which is much smaller than Ryugu's size ($1.04 \times 1.02 \times 0.88$ km; Watanabe et al., 2019). Thus, we can treat the close-up images as plane surfaces.

We estimate the apparent three-axial lengths of small blocks. Firstly, approximating the outlines of small blocks as ellipses, the apparent long (a') and short axes (b') of small blocks are measured using the SAOImage DS9 software. The diameter of a small block is defined as its mean horizontal dimension, which is the arithmetic mean of its apparent long and short axes, $\frac{a'+b'}{2}$.

Next, the heights of small blocks are investigated by measuring the maximum length of their horizontal shadows on the images using SAOImage DS9, considering emission, incidence and phase angle of each pixel. As shown Fig. 1, taking account of the position of the Sun and the spacecraft, the height (h) of the small blocks is determined by $h = \frac{l}{\tan i + \tan e}$, where l , i and e are the apparent shadow length, the solar incidence angle, and the emission angle, respectively. The pixel scale and incidence angle for each small block are averaged across the surface of the image. The emission angle is calculated from the position of each small block. That is, assuming $e = 0$ at the center line $x = \frac{L}{2}$, we obtain $\tan e = \frac{x_1 - \frac{L}{2}}{H}$, where x_1 is the x -coordinate of the sunward edge of the shadow, H is the altitude of the spacecraft and L is the width of the close-up image (Fig. 1). The values of $\tan e$ are small, ranging from 0.055 to -0.055 because the geometry of the close-up images we used tends to follow $L/H = 0.11$. Once the values of a' , b' and h for each small block have been obtained, they are arranged in size order from largest to smallest to determine a , b , and c ($a \geq b \geq c$).

For determining shadow length, we treat pixels with a luminosity below a certain threshold value as shadow, so shadow length largely depends on this threshold value. In this study, the luminosity threshold value is defined as the mid-way point between the brightest and darkest peaks in the luminosity pixel distribution of the image. For more detail, see Section 3.1.

We focus our study on apparent three-axial lengths of small blocks with diameters between 5.0 cm and 7.6 m from the eight close-up images taken at altitudes ranging from 31 m to 461 m on 10th and 11th July 2019, obtained immediately before the second touch-down of the Hayabusa2 spacecraft (Fig. 2 and Fig. 3). These close-up images are selected because of their large incidence angle (37.5°), and incidence angles larger than 30° are considered to be necessary for estimating the heights of the blocks accurately (see Appendix A). The heights of small blocks tend to be underestimated (see Fig. A1 in Appendix A) using this method if the incidence angles are small, i. e. $< 30^\circ$. Unfortunately, close-up images at altitudes below 500 m and incidence angles larger than 30° are only available for the second touch-down sequence and its rehearsal sequence. Moreover, the images obtained during these sequences cover broadly the same area and/or somewhat overlap each other. Therefore, the area covered by close-up images of the second touch-down sequence is the only one suitable. Thus, in order to expand the block shape dataset to other regions, several close-up images with incidence angles $\sim 14^\circ$ (except for region 455) at different latitudes are analyzed (Fig. 2 and Fig. 10).

When the heights of many blocks are estimated from their shadow lengths, it is essential to identify geomorphological surface variations and the shapes of small blocks more clearly. In particular, many shadows do not cover enough pixels to estimate block heights in the original image because the blocks' shadow lengths are generally shorter than the blocks' heights (and much smaller than the apparent lengths a' and b'). This introduces a certain degree of inaccuracy into the heights of many blocks estimated from the shadow lengths of the original image. From a statistical point of view, sub-pixel scale is desirable for accurate height measurement, so we enlarged the image array size from 1024×1024 pixels to 4096×4096 pixels with a bilinear interpolation using the software ImageJ. An example before and after the bilinear interpolation of an image is shown in Fig. 4 (top). It illustrates that the quality of the bilinear interpolation image is improved over the original image.

The shadow length depends on the quality of the image. So, in order to confirm the quality of the image using bilinear interpolation, a few images are corrected using image deconvolution (see Gaddis et al., 1995). Fig. 4 (top) shows an example of original, bilinear interpolation and deconvoluted images for comparison. For the deconvoluted image, as the observed images were blurred by the point-spread function of the imaging system, the Richardson-Lucy algorithm (Richardson, 1972; Lucy, 1974) can be used to recover the original image (Ishiguro et al., 2010). The image restoration algorithm yields good results, improving the image resolution. Fig. 4 (bottom) shows the luminosity profiles by pixel along the lines for each image. As these profiles are similar, we concluded that the quality of the image using bilinear interpolation is similar to that of the deconvoluted image in terms of measured shadow length. In this study, we use the bilinear interpolation images (4096×4096 pixels) to investigate the three-axial lengths of blocks. The pixel scales of the eight close-up images range from 0.83 mm to 12 mm using the bilinear interpolation.

As described above, for accurate measurement, shadows need to extend over a sufficient number of pixels. At incidence angle 37.5° and quadruple resolution of the original image, the shadows of almost all blocks larger than 60 pixels in diameter are found to be at least 8 pixels long. Therefore, the shadow lengths of blocks larger than 60 pixels in diameter are measured in the eight close-up images used in this study.

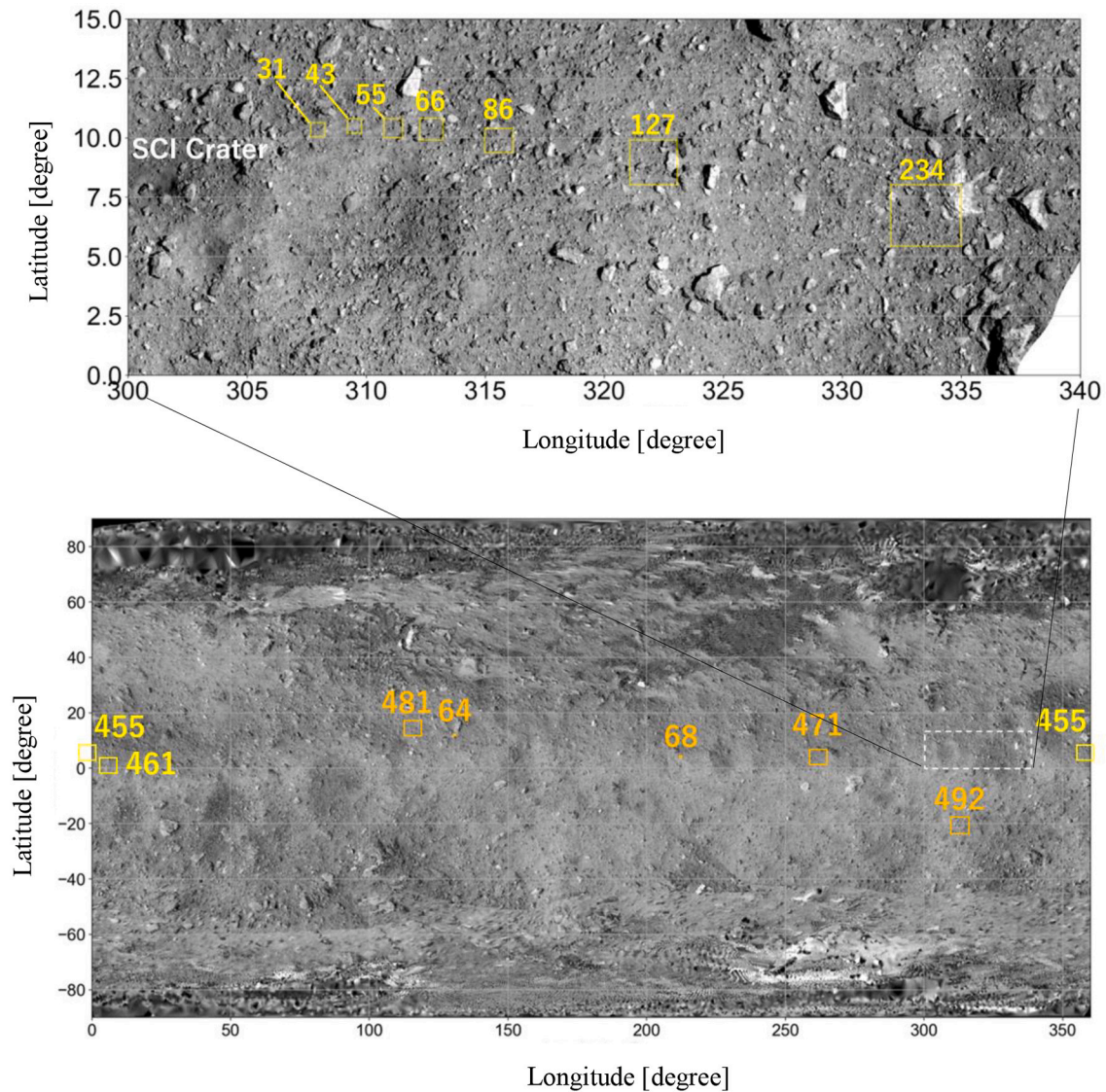


Fig. 2. Overview of Ryugu’s surface indicating those regions where small blocks were counted for this study. The upper image indicates the selected images acquired on 11th July 2019, immediately before the second touch-down of the Hayabusa2 spacecraft. The lower image (taken from [Cho et al., 2021](#)) shows several arbitrarily selected regions on the surface of Ryugu. The numbers refer to regions shown in [Fig. 3](#) and [Fig. 10](#). Yellow squares show the regions where incidence angles were higher than 30° at the time of observation, while orange squares indicate an incidence angle lower than 15°. (For interpretation of the references to colour in this figure legend, the reader is referred to the web version of this article.)

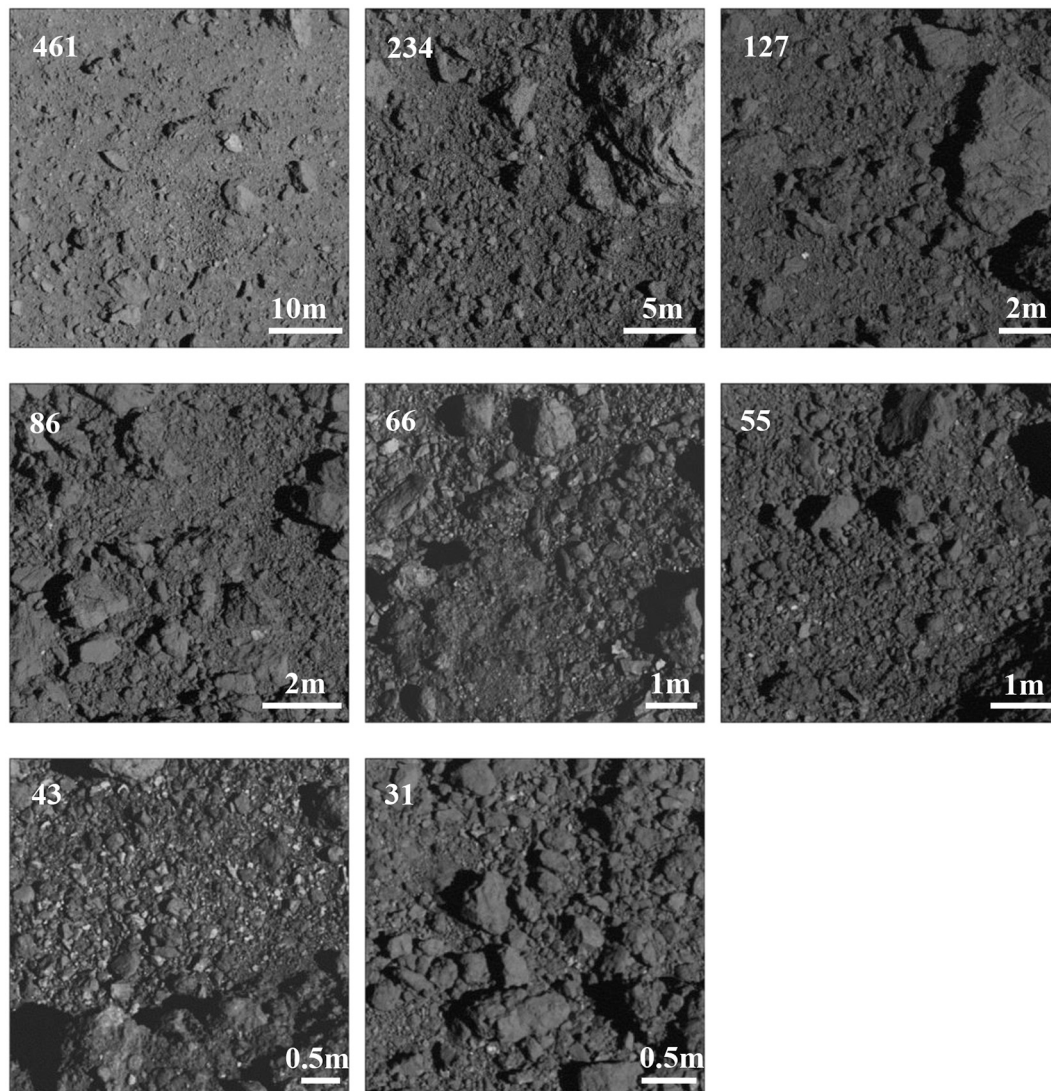


Fig. 3. Eight close-up images acquired on 10th and 11th July 2019, immediately before the second touch-down of the Hayabusa2 spacecraft. Region numbers and IDs: (461) `hyb2_onc_20190710_232532_tvfl2c.fit`, (234) `hyb2_onc_20190711_000708_tvfl2c.fit`, (127) `hyb2_onc_20190711_002204_tvfl2c.fit`, (86) `hyb2_onc_20190711_003036_tvfl2c.fit`, (66) `hyb2_onc_20190711_003420_tvfl2c.fit`, (55) `hyb2_onc_20190711_003628_tvfl2c.fit`, (43) `hyb2_onc_20190711_003836_tvfl2c.fit`, (31) `hyb2_onc_20190711_004044_tvfl2c.fit`. Region numbers are given to the top left for each image and give the altitude the corresponding image was taken at in m. The location of each image on Ryugu's surface is shown in Fig. 2. Scale bars are indicated to the lower right.

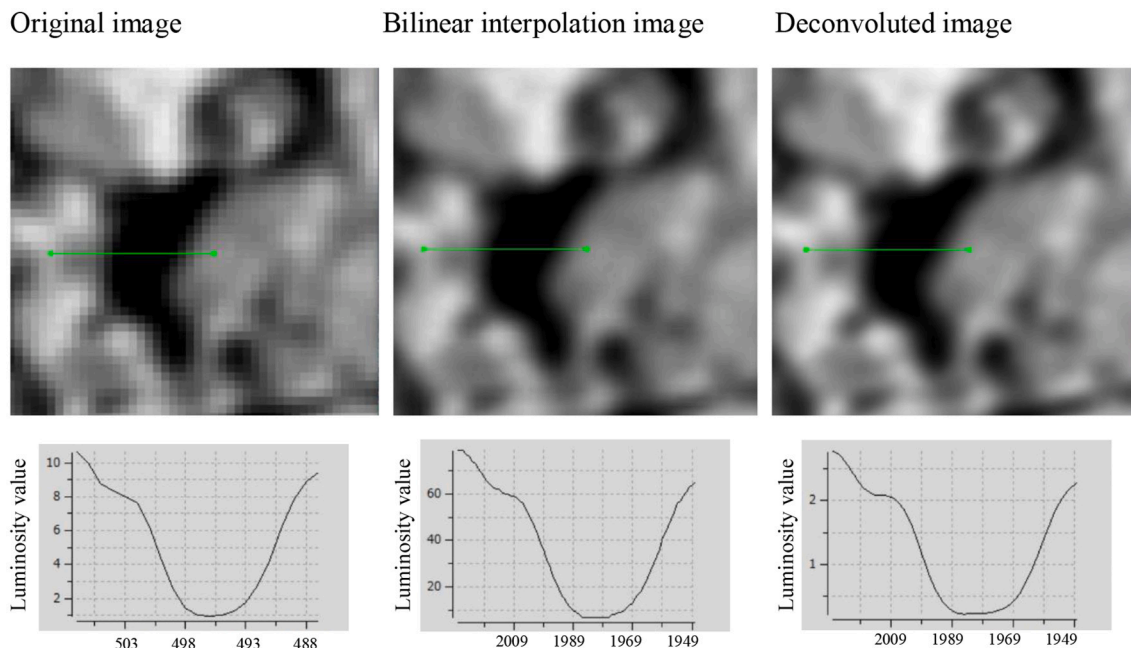


Fig. 4. Top: original, bilinear interpolation and deconvolved images of the central part of region 43 (hyb2_onc_20190711_003836_tvf_l2c.fit). The bilinear interpolation image is obtained using the software ImageJ. The deconvolved image with five iterations is obtained using the Richardson-Lucy algorithm. The luminosity value ranges are 0–35.1 for the original image, 0–255 for the bilinear image and 0–9.16 for the deconvolved image. The length of line in each image is 9.3 cm (20 pixels for the original image, 80 pixels for the bilinear interpolation and deconvolved images).

Bottom: luminosity profiles by pixel along the lines. The vertical and horizontal axes show the luminosity value and the x-coordinate corresponding to the line, respectively. The scales of the vertical axes correspond to the relative luminosity values. In this study, all boulders are measured using the bilinear interpolation images. In the case of region 43, a luminosity threshold value of 38 is adopted for the bilinear image, i.e. pixels below the threshold value 38 are treated as shadows.

3. Observational results

3.1. Correlation between block heights and shadow threshold

As mentioned before, the shadow length largely depends on the luminosity threshold value for each image. The luminosity threshold value in this study is defined as the mid-way point between the brightest and darkest peaks in the pixel luminosity distribution of the image. The choice of these values is, however, affected by errors. Therefore, we start by evaluating the correlation between the heights of blocks and the shadow threshold using the image of region 86 [ID: hyb2_onc_20190711_003036_tvf_l2c.fit]. We chose this image because it was taken at an intermediate altitude of the eight images from the second touch-down sequence we analyzed.

On the bilinear interpolation image of region 86, nearly one thousand blocks with diameters of 0.06 m to 2.44 m are measured by elliptic approximation and the heights of 544 blocks with diameters of 0.14 m (corresponding to 60 pixels on the bilinear interpolation image) to 2.44 m are derived from their shadow lengths (Table 2).

Fig. 5 shows the histograms of b/a and c/a of 544 blocks for the luminosity threshold values of 24, 27, 30, 33 and 36 brightness value (BV) on an 8-bit gray scale. Mean c/a ratios increase with increasing luminosity threshold, while mean b/a ratios remain approximately constant, although a slight increase with luminosity threshold is also noticeable here. In other words, small (i.e. < 0.4) c/a ratios decrease with increasing luminosity threshold whilst the shapes of the histograms of b/a are somewhat similar, regardless of luminosity threshold.

In this image, the appropriate threshold value is considered to be 30 based on the brightest and darkest peaks in the luminosity pixel distribution of the image. The error of the threshold value due to selection bias is 10% because the brightest peak is rather wide. This translates into a threshold range from 27 to 33. Converting the error in threshold value into an error in the mean axial ratios, we arrive at mean b/a and c/a ratios of 0.71 ± 0.01 and 0.46 ± 0.03 for these blocks. In this study, the errors in the estimates of mean axial ratios for each image are thus considered to be ± 0.01 for b/a , and ± 0.03 for c/a .

As described above, when determining a , b and c , we arranged blocks in order of size based on apparent lengths a' and b' obtained from the elliptic approximation, and height h obtained from their shadow lengths. The heights h of some blocks are larger than the apparent lengths a' and/or b' . We suspected this to have to do with the way some blocks are tilted. That is because there is a possibility that the three axial lengths cannot be precisely estimated using the method of this study when blocks are extremely tilted to the surface. In order to investigate this effect, the proportion of blocks with $h > a'$ and $h > b'$ are investigated (Fig. 6). For a threshold value of 30, only a small number of blocks have $h > a'$ (7% of the total) and $h > b'$ (15% of the total), indicating that these small proportions do not influence the block size and shape distributions (a similar tendency is observed for other regions (see Table 2)). In fact, the power-indices of the block size distribution are similar regardless of luminosity threshold value (ranging from 24 to 36).

Table 2

Regions investigated and observational results of small blocks (i.e. small boulders, cobbles and pebbles) on Ryugu. The power-indices of cumulative boulder size distributions using the minimum diameters (D_{min}) are obtained by combining a maximum-likelihood fitting method with goodness-of-fit tests based on the Kolmogorov-Smirnov statistic, as proposed by [Clauset et al. \(2009\)](#) and [Tancredi et al. \(2015\)](#). The cumulative boulder size distribution is expressed as $N(>D) = CD^\alpha$, where D is the boulder diameter, α is the power-index and C is a constant.

The maximum-likelihood indicator of the power-index α can be calculated as

$$\alpha = \frac{n}{\sum_{i=1}^n \ln \frac{D_i}{D_{min}}}$$

where D_i , $i = 1, 2, 3, \dots, n$, are the observed values of the diameters ($D_i \geq D_{min}$), and n is the total number of boulders larger than D_{min} . In order to obtain the minimum diameter, we compute the Kolmogorov-Smirnov statistic for different values of D_{min} , which is simply the maximum distance between the data of the cumulative size distribution and the fitted model; the estimate D_{min} is the value of D_{min} that minimizes this distance ([Tancredi et al., 2015](#)). Italic numerical values mean reference data because of small number of blocks.

Region	Image ID	Solar incidence angle [degree]	Counted number of blocks as elliptic approximation	Size range of blocks as elliptic approximation [m]	D_{min} [m]	Number fitting n	Power-index α	Error bar of α	Counted number of blocks with the three axial lengths	Size range of blocks with the three axial length [m]	Mean b/a ratio	Mean c/a ratio	Ratio of $h > a'$ [%]	Ratio of $h > b'$ [%]
Second Touch-down sequence														
	461	37.54	2299	0.18–7.62	0.74	414	2.22	0.11	413	0.74–7.62	0.69	0.39	0	5
	234	37.54	859	0.18–4.69	0.56	234	2.53	0.17	452	0.38–4.69	0.73	0.45	3	7
	127	37.54	891	0.09–5.80	0.26	319	2.18	0.13	470	0.20–5.80	0.71	0.44	5	10
∞	86	37.54	1002	0.06–2.44	0.13	600	1.80	0.08	544	0.14–2.44	0.71	0.46	7	15
	66	37.54	1150	0.04–1.45	0.17	258	2.38	0.15	606	0.11–1.45	0.72	0.47	10	17
	55	37.54	1192	0.03–1.48	0.17	223	2.73	0.19	707	0.09–1.48	0.71	0.46	6	14
	43	37.54	853	0.024–0.754	0.13	145	3.13	0.26	466	0.070–0.754	0.72	0.46	9	16
	31	37.54	629	0.024–0.865	0.08	299	1.81	0.11	466	0.050–0.865	0.71	0.46	8	15
Other regions														
	455	30.37	698	0.33–6.71	0.63	389	2.08	0.11	292	0.73–6.71	0.71	0.39	1	7
	471	14.49	348	0.47–4.24	1.01	142	2.90	0.25	24	2.04–4.24	0.73	0.41	4	4
	481	14.27	741	0.33–7.40	0.80	383	2.19	0.12	48	2.11–7.40	0.67	0.38	0	10
	492	12.53	654	0.38–7.02	0.78	395	2.16	0.11	30	2.51–7.02	0.68	0.33	0	3
	64	14.28	463	0.04–1.31	0.11	226	2.06	0.14	35	0.27–1.31	0.72	0.44	0	11
	68	14.50	407	0.05–4.10	0.13	174	1.87	0.15	41	0.29–4.10	0.71	0.45	0	7

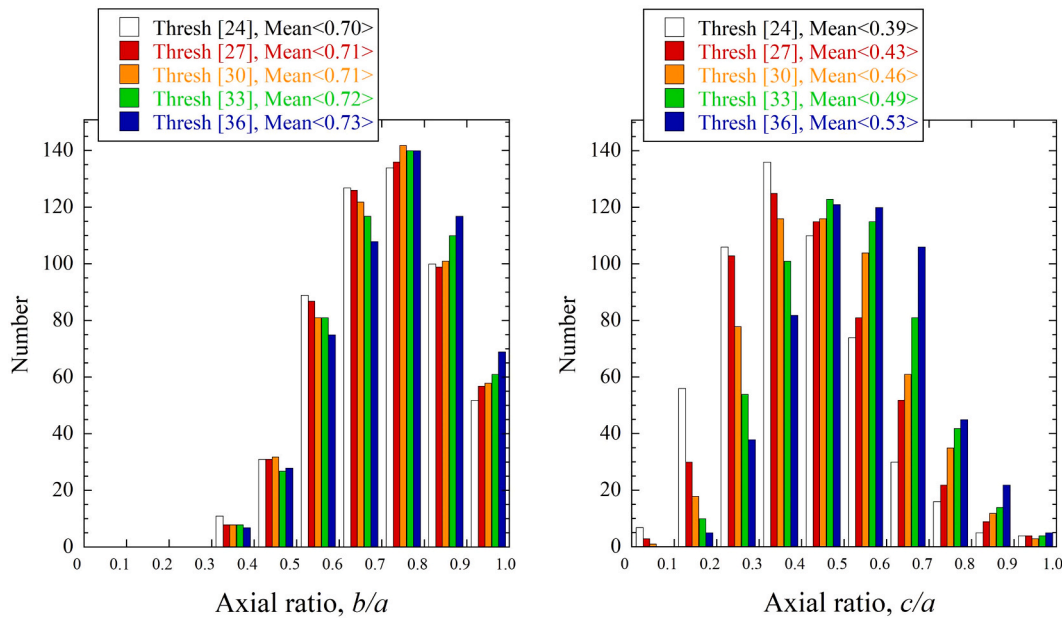


Fig. 5. Histograms of axial ratios b/a and c/a of the 544 blocks with diameters of 0.14 m to 2.44 m in region 86 [ID: hyb2_onc_20190711_003036_tvf_l2c.fit]. The luminosity threshold values and mean axial ratios are illustrated in square and angle brackets, respectively. (For interpretation of the references to colour in this figure legend, the reader is referred to the web version of this article.)

3.2. Block size distributions in the eight close-up images

The numbers of blocks counted are given in Table 2. In this study, the apparent lengths a' and b' of nearly 8900 blocks in the eight close-up images were measured first. After that, the heights of the blocks larger than 60 pixels on the bilinear interpolation images were measured, resulting in a total of ~4100 blocks whose three axial lengths had been obtained. As mentioned before, several close-up images with incidence angles ~14° (except for region 455) at different latitudes are additionally analyzed to underpin the block shape dataset for other regions (Fig. 10). This adds another ~3300 blocks with known a' and b' , for 470 of which we were able to measure three-axial ratios.

Fig. 7 shows the cumulative small block (small boulder, cobble and pebble) size distributions per unit area in the eight close-up images

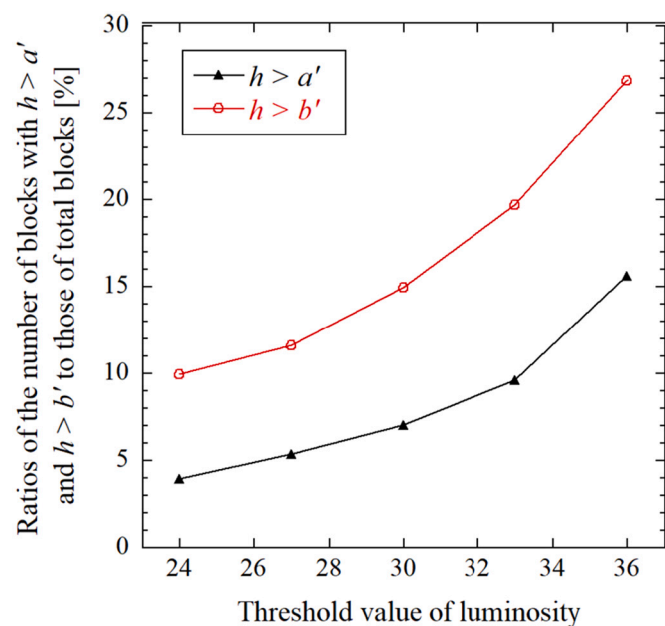


Fig. 6. Correlation between the luminosity threshold value and the ratios of the number of blocks with $h > a'$ and $h > b'$ to those of total blocks in region 86.

preceding second touch-down (nearly 8900 blocks). The cumulative size distributions do not appear to form a straight line, meaning that the number density of blocks is somewhat different in each region. For deriving the power-index of the block size distribution we follow Clauset et al. (2009), who suggest combining a maximum-likelihood fitting

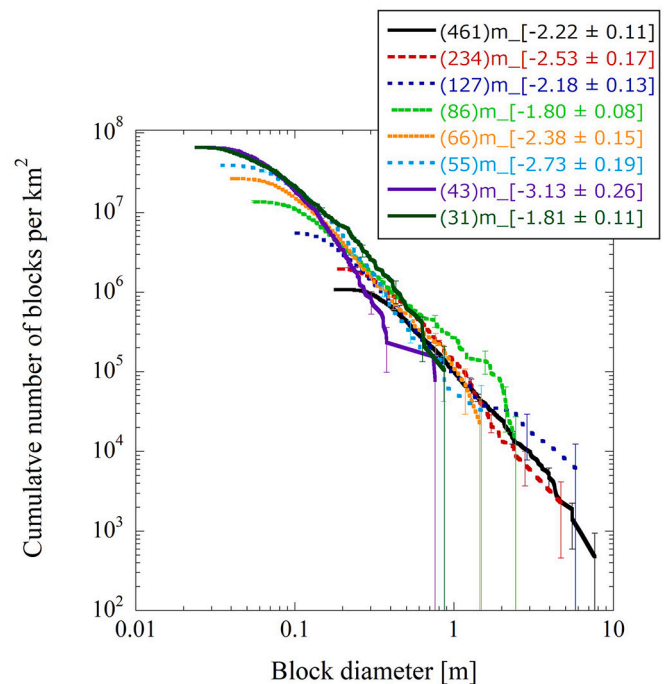


Fig. 7. Cumulative small block (small boulder, cobble and pebble) size distributions per unit area in the eight close-up images (on 10th and 11th July 2019) obtained immediately before Hayabusa2's second touch-down. The altitude of the spacecraft, corresponding to the region number show in Fig. 3, is given in parentheses. The power-index for each size distribution is shown in square brackets. Vertical error bars indicate the root of the cumulative number of small blocks divided by the corresponding area on Ryugu. Error bars are restricted to only a few points to improve legibility. (For interpretation of the references to colour in this figure legend, the reader is referred to the web version of this article.)

method with goodness-of-fit tests based on the Kolmogorov-Smirnov statistic and likelihood ratios. The power-indices of the block size distributions range from -1.80 ± 0.08 to -3.13 ± 0.26 . The power-index of the block size distribution shows no tendency to vary over the size range of the blocks. This diverges from Michikami et al. (2019), who measured the sizes of small blocks (0.02 to 9.1 m in diameter) on five close-up images of Ryugu near 130° E and suggested that the slope (power-index) of the size distribution gradually decreases with decreasing block size. The discrepancy between these observations will be discussed in Section 4.2.

3.3. Block shape distributions in the eight close-up images

As mentioned above, we measure the shadow lengths of small blocks with >60 pixels in diameter in each image and estimate their heights from their shadows, resulting in height estimates of nearly 4100 small blocks with diameters of 5.0 cm to 7.6 m (Table 2). Fig. 8 shows the

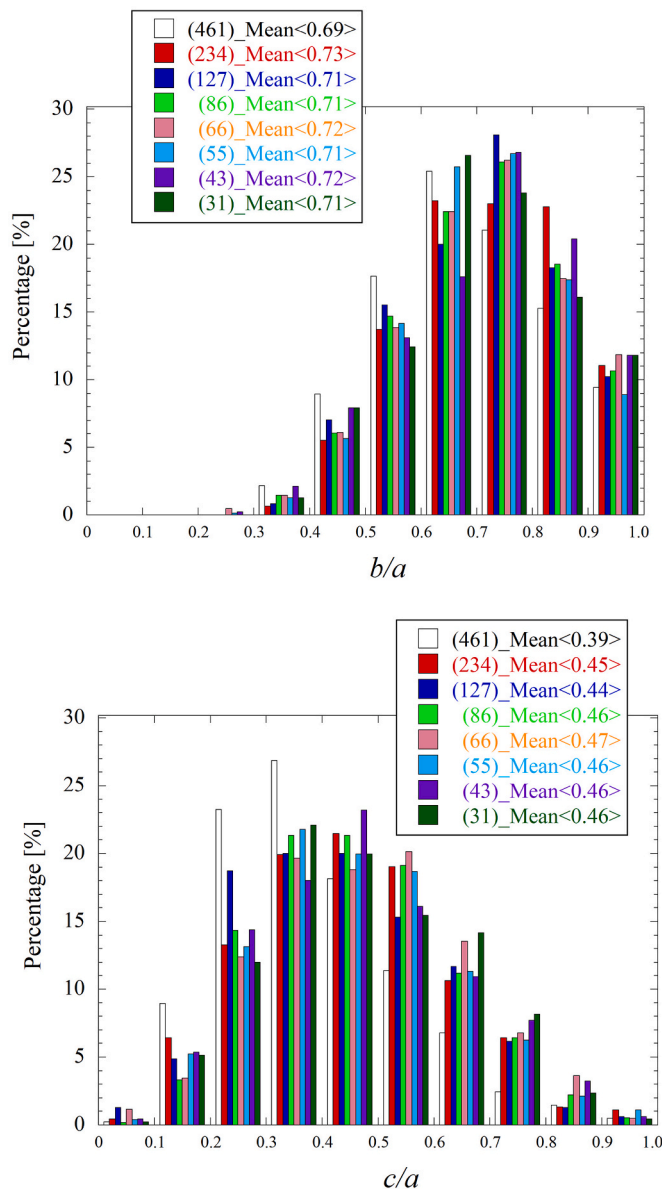


Fig. 8. Histograms of axial ratios b/a and c/a of the small blocks with diameters of 5.0 cm to 7.6 m in the eight close-up images obtained before Hayabusa2's second touch-down. Block number counts for the bins are normalized to the total number of blocks. The region number and the mean axial ratios are illustrated in parentheses and angle brackets, respectively. (For interpretation of the references to colour in this figure legend, the reader is referred to the web version of this article.)

histograms of axial ratios b/a and c/a of the small blocks on the above-mentioned close-up images. The mean b/a ratios of small blocks for all regions are similar, approximately 0.7, resembling the mean b/a ratios of laboratory impact fragments (Fujiwara et al., 1978; Capaccioni et al., 1984, 1986; Michikami et al., 2016, 2018). In addition, except for region 461, the shapes of the histograms for the axial ratio b/a are also similar regardless of size range. Using a Kruskal-Wallis test, a suitable test for confirming the difference between more than two statistical populations with non-normal distributions, we determine the p -value among these mean b/a ratios. p is 0.014 including region 461 and 0.390 if region 461 is excluded, which implies that the differences among the b/a ratios including region 461 are statistically significant at the 95% confidence level whilst this is not the case if region 461 is excluded.

The mean c/a ratios of small blocks for the seven regions excluding region 461 are similar, approximately 0.46, almost the same as for laboratory impact fragments. In region 461, the mean c/a ratio of 0.39 differs from the other regions. The shape of the histogram for the axial c/a ratio in this region also differs from the others and the peak of the histogram shifts towards smaller values, meaning that the heights of the small blocks are relatively small compared with their diameters. In a Kruskal-Wallis test, the p -values among these mean c/a ratios including and excluding region 461 are less than 10^{-4} and 0.097, respectively, so the differences among the c/a ratios including region 461 are statistically significant at the 95% confidence level but not significant if the region is excluded. In conclusion, in seven of the eight regions observed at altitudes below 250 m, the mean axial b/a and c/a ratios of the small blocks and their shape distributions are similar, whilst region 461 represents an exception.

The above results could indicate a correlation between sizes and apparent shapes of small blocks. To confirm this, we divide the sizes of small blocks for each region into three size ranges and investigate the correlation between the sizes and the c/a ratios of small blocks in Fig. 9. Blocks several meters in diameter appear to have low c/a ratios. By contrast, blocks with diameters below approx. 1 m have similar c/a ratios, regardless of their sizes. We will discuss this observation in Section 4.1.

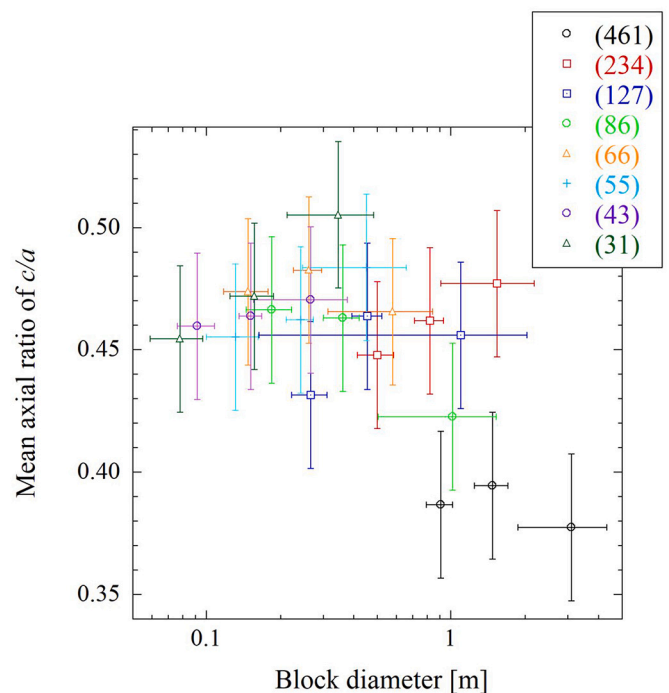


Fig. 9. Diagram of mean c/a ratios vs. block representative diameter for a given size range in the eight close-up images preceding second touch-down. The blocks considered in each region are divided into three size ranges in order of increasing size: first 50, then 100 and then the rest of blocks for each bin. The region numbers are given in parentheses. (For interpretation of the references to colour in this figure legend, the reader is referred to the web version of this article.)

4. Discussion

4.1. Block shapes – a global perspective

Revisiting Fig. 9, the mean c/a ratios of the blocks several meters in diameter seem to be smaller than for blocks less than 1 m in size. To confirm this result, we obtained new data of the other regions 64, 68, 455, 471, 481 and 492 (see Fig. 2 and Fig. 10; for more detail, also see Table 2) at different latitudes, and investigated the c/a ratios of their blocks. The image of region 455 has a relatively large incidence angle of 30.4° , and the shadow lengths of 292 blocks larger than 60 pixels in diameter (in the bilinear interpolation image) are measured.

The images of regions 64, 68, 471 and 481 have relatively small incidence angles of $\sim 14^\circ$, hence we measured the shadow lengths of blocks larger than 160 pixels in diameter (in the bilinear interpolation image). At 12.5° , the incidence angle of the image of region 492 is also small. Consequently the shadow lengths of blocks larger than 190 pixels in diameter (in the bilinear interpolation image) were measured here. In each region, we count fewer than 50 blocks, which is not enough for reliable statistics on the c/a ratio (Table 2). Furthermore, we cannot rule out the possibility that the c/a ratios of these blocks are underestimated due to lower incidence angles ($< 15^\circ$). Thus, we treat these as reference data.

Fig. 11 covers the combined dataset, i.e. the data of Fig. 9 combined with the above data of the other regions. It shows the correlation between the sizes and the mean c/a ratios of small blocks in the eight close-up images preceding second touch-down and six more close-up images at different latitudes. The mean c/a ratios of the blocks in the regions 64 and 68 derived from our measurements are 0.44 and 0.45, respectively, so the shapes of blocks, mostly smaller than 1 m, resemble laboratory impact fragments. By contrast, the mean c/a ratios of larger blocks several meters in size in the regions 471, 481 and 492 are small: 0.41, 0.38 and 0.33, respectively. In region 455, the mean c/a ratios of blocks ranging from 0.73 m to 6.71 m is 0.39, and the mean c/a ratio of 50 blocks larger than

1.68 m is 0.33. Therefore, it is likely that the mean c/a ratio of several-meter-sized blocks on Ryugu is relatively small compared with blocks smaller than 1 m and laboratory impact fragments. In other words, larger blocks seem to be flatter.

Most blocks seem to lie flat on the surface, as the proportions of blocks with $h > a'$ and $h > b'$ are similar and small (Table 2), suggesting that their c axes are orientated vertically (Note that blocks' apparent shapes are not affected by their orientations).

Why is the mean c/a ratio for the larger blocks smaller than for laboratory impact fragments? One possible explanation is that the larger blocks may have been produced by a weak disruption. For instance, according to the laboratory impact experiments of Michikami et al. (2016), relatively flat fragments with a mean $c/a \sim 0.38$ are produced by a weak disruption of a monolithic target (shot s2131 in their study). However, asteroid Ryugu is not a monolithic body but a rubble-pile structure (Watanabe et al., 2019), and little is known on the fragment shapes in cratering and disruptions on rubble piles. We will discuss this in Section 4.2.

A more plausible explanation is that some of the larger blocks in the equatorial region are partly or mostly buried in the fine-grained material and/or small blocks (< 1 m) as suggested by Sugita et al. (2019), Michikami et al. (2019) and Tanabe et al. (2021). As shown in Fig. 4e of Michikami et al. (2019), the typical size of partly buried blocks is considered to be several meters although such buried boulders are hard to find in the images. Tanabe et al. (2021) obtained a global distribution of boulders larger than 0.75 m on Ryugu using a new method that automatically measures the abundance of small blocks resolved at less than a few pixels by quantifying the surface radiance variation during the spinning of the asteroid. They show that, in the equatorial region, blocks smaller than 1 m are abundant, while those larger than 1 m are less abundant. This is consistent with the observation that the number density of blocks larger than 5 m in the equatorial region is relatively small compared with mid and high latitudes (Sugita et al., 2019; Michikami et al., 2019).

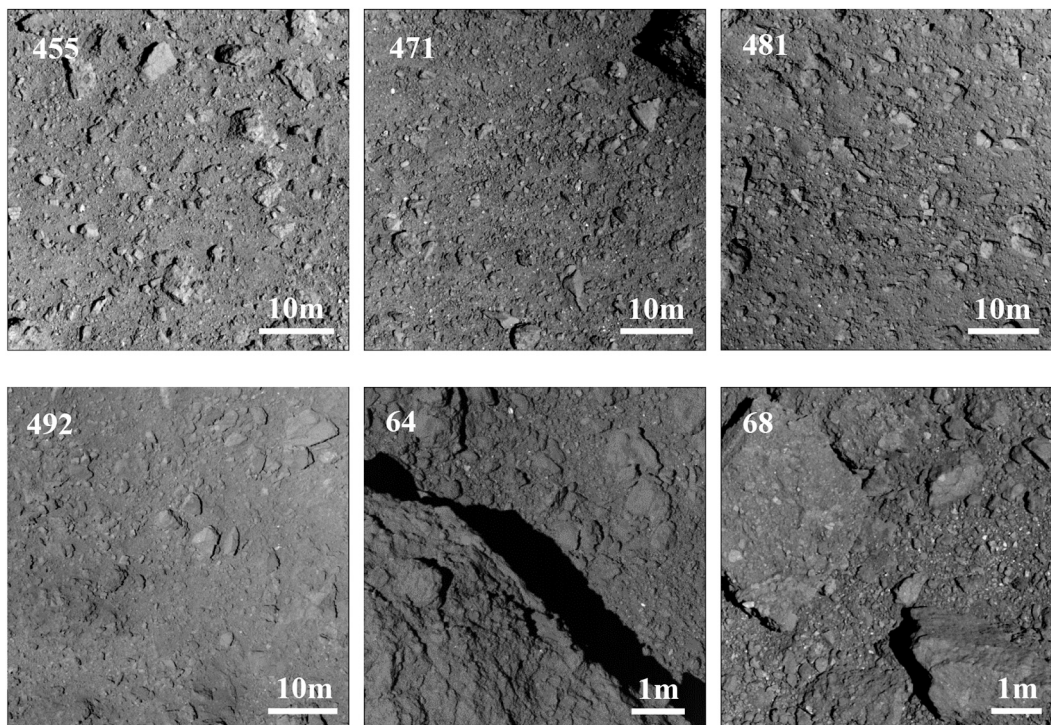


Fig. 10. Six close-up images for other regions on Ryugu. Region number and IDs: (455) hyb2_onc_20190516_011850_tvf_l2c.fit, (471) hyb2_onc_20190221_205818_tvf_l2c.fit, (481) hyb2_onc_20180921_042418_tvf_l2c.fit, (492) hyb2_onc_20181003_021748_tvf_l2c.fit, (64) hyb2_onc_20180921_040402_tvf_l2c.fit, (68) hyb2_onc_20190221_220322_tvf_l2c.fit. The region number on the top left for each image corresponds to altitude [m]. The position of each image is shown in Fig. 2. Scale bars are indicated to the lower right.

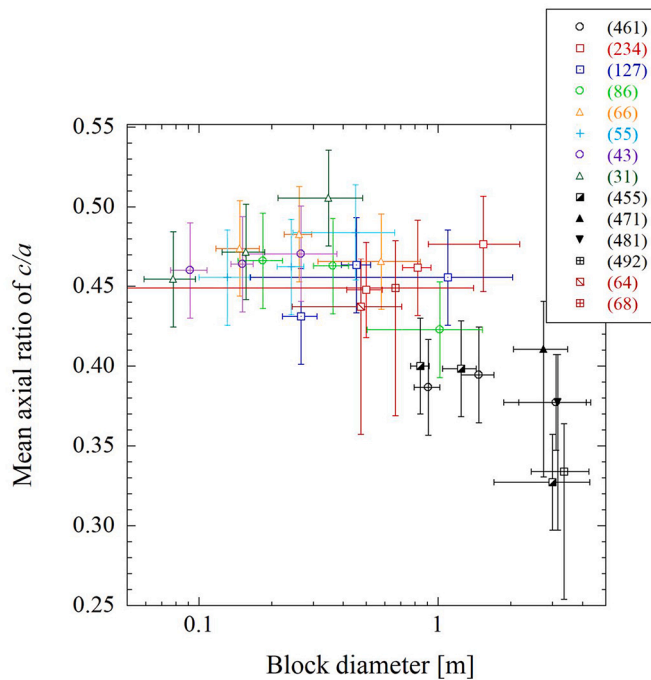


Fig. 11. Diagram of mean c/a ratios vs. block representative diameter for a given size range in the eight close-up images preceding second touch-down and other six close-up images at different latitudes. The blocks in each region except for regions 64, 68, 471, 481 and 492 are divided into three size ranges in order of increasing size: first 50, then 100 and then the rest of blocks for each bin. The blocks for regions 64, 68, 471, 481 and 492 are treated as one bin because numbers were small. The region numbers are given in parentheses. (For interpretation of the references to colour in this figure legend, the reader is referred to the web version of this article.)

Cho et al. (2021) also investigated the crater morphology on Ryugu in more detail and suggested that a layer of fine grained material few meters thick exists between the surface and the deep subsurface. This implies that some blocks smaller than 1 m can be mostly buried in the fine grained materials within this layer, while some blocks with sizes of several meters can only be partly buried. In fact, the SCI impact experiment indicated that the Iijima boulder, several meters in size, was excavated by the impact (Arakawa et al., 2020).

Moving away from Ryugu, Jawin et al. (2020) investigated the global patterns of recent mass movement on asteroid Bennu and found that mass movement altered the surface expression of large (≥ 30 m diameter) blocks, burying them in the equatorial region.

From the above it is clear that some blocks several meters in size must be partly buried, and the actual mean c/a ratios of blocks in this size range must be larger than the measured values.

Finally, in the seven images we investigated, the mean b/a and c/a ratios of the smaller blocks in the range from a few cm to several m are 0.71 and 0.46, respectively, which is consistent with laboratory impact fragments (Michikami et al., 2016).

4.2. Block shapes – a local perspective

As described before, Michikami et al. (2019) suggested that the slope (power-index) of the size distribution gradually decreases with decreasing block size, based on the measurement of small blocks on five close-up images of Ryugu near 130° E. However, in the eight regions of this study, such a tendency is not found. It is possible that the localized topography affects the migration of small blocks. In addition, the power-index of the block size distribution can also be considered an indicator of the fragmentation in that a steeper index is indicative of a greater degree of fragmentation (Hartmann, 1969; Thomas et al., 2001). Therefore, to

understand the migration and/or formation of small blocks on the localized topography, we examine how the power-indices of the blocks' size distributions are correlated with block size ranges and block shapes.

Fig. 12 shows the relation between the block sizes and the power-indices of the size distributions. In Fig. 12, in order to increase the block size of the data set, we added the data of regions 64, 68, 455, 471, 481 and 492 to the data of the second touch-down sequence, and combined them with the local and global data of Michikami et al. (2019). Although the power-index seems to increase as the block size (D_{\min} , see the caption of Table 2) increases, this trend is weak, with a correlation coefficient of only 0.45. In particular, the power-indices of regions 43, 55, 66, 234 and 471 deviate from this trend in that they are comparatively large. In the following, we speculate on several causes of the spread in the power-index.

It should be noted that regions 31, 43, 55 and 66 are at the rim of a crater (6° N, 309° E, 77.1 m in diameter; Cho et al., 2021), and, with the exception of region 31, their power-indices are steeper than those for other regions 86, 127 and 461. Typical craters larger than several tens of meters on Ryugu are outlined by blocks remaining on the rim (e.g. Cho et al., 2021). These small blocks can be expected to be related to the formation of the impact crater, with several possible explanations regarding their origin. As one possibility, the blocks inside the crater before an impact are mobilized and concentrated near the crater rim during the crater's formation (e.g. Honda et al., 2021). For instance, when the artificial impact crater on Ryugu was formed by Hayabusa2's Small Carry-on Impactor SCI (Arakawa et al., 2020), numerous boulders moved towards near the crater rim (Honda et al., 2021). As another possibility, these small blocks could be the product of the impact process itself. For instance, almost all blocks on Eros are the product of impact cratering, with a size distribution power-index of almost -3.3 (e.g.

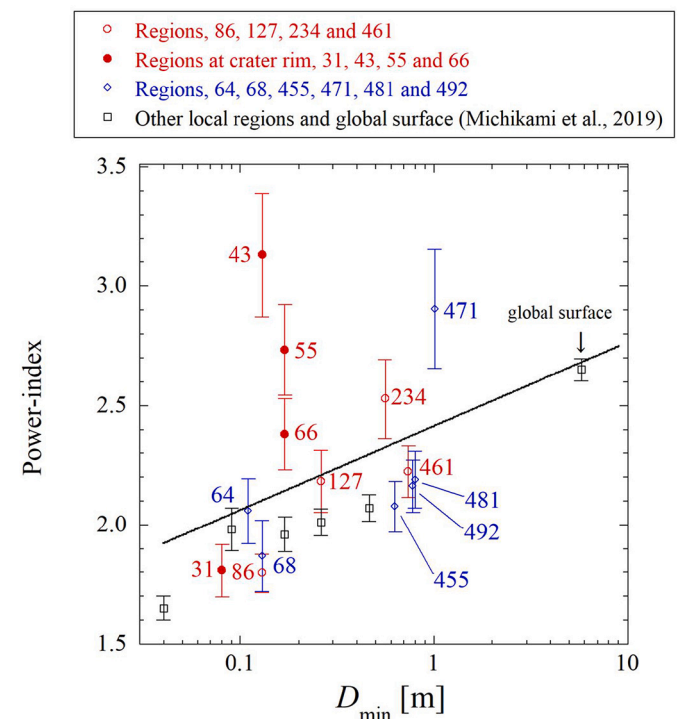


Fig. 12. Relation between the power-indices of the cumulative block size distributions in several local regions and for the global surface of Ryugu and the D_{\min} (see the caption of Table 2) of the small blocks. Note that the data of Michikami et al. (2019) has been added to this data. The black line corresponds to the best fit function for the data set. Region numbers of the second touch-down sequence and other local regions in this study are shown in red and blue, respectively. The data lists are shown in Table 2. (For interpretation of the references to colour in this figure legend, the reader is referred to the web version of this article.)

Dombard et al., 2010; Michikami and Hagermann, 2021), which is steeper than the global value of -2.65 ± 0.05 observed on the surface of Ryugu (Michikami et al., 2019) and the global value of -3.05 ± 0.14 on Itokawa (Michikami et al., 2008; Michikami and Hagermann, 2021). Most blocks on Ryugu and Itokawa are likely to be primarily products of the catastrophic disruption of a larger parent body. The blocks in regions 43, 55 and 66 (and possibly 234 and 471) may have been comminuted by later impact cratering, resulting in a steeper size distributions.

Another possibility for the high abundance of small fragments and the corresponding steep size distribution is thermal fatigue caused by the day-night temperature cycles on asteroid surfaces, which can act to break down rocks into smaller fragments (Delbo et al., 2014; Molaro et al., 2020; Cambioni et al., 2021). However, the minimum size of particles forming the regolith layers on Ryugu is in the cm range (Sugita et al., 2019; Watanabe et al., 2019), which appears to be larger than the \sim mm minimum size of particles on Itokawa (Yano et al., 2006) and Eros (Veveřka et al., 2001). Both locally (Grott et al., 2019) and globally (Okada et al., 2020), boulders on Ryugu tend to have very low thermal inertia values in the lower $10^2 \text{ J}\cdot\text{m}^{-2}\cdot\text{K}^{-1}\cdot\text{s}^{-0.5}$ range, which translates into diurnal skin depths of only a couple of mm. Therefore, explaining the relative abundance of fragments in the cm-size range on Ryugu by thermal fatigue is not straightforward. Moreover, it is difficult to give reasons for why thermal fatigue should primarily affect regions 43, 55 and 66. Cambioni et al. (2021) also highlight the reduced effectiveness of thermal fatigue in highly porous blocks as they are found on Ryugu. It should also be added that, although signs of in-situ disaggregation and exfoliation are widely observed on asteroid Bennu (Molaro et al., 2020), this does not seem to be the case on Ryugu. Further quantitative studies comparing the effects of thermal fatigue and (lower-energy) impacts on the highly porous blocks on Ryugu will be crucial for a better understanding of fine-regolith production.

Of course, one explanation for the wide scatter of power-indices across the blocks' size range shown in Fig. 12 could be that the small blocks form several distinct populations. According to Michikami et al. (2019), the migration of small particles (including cobbles and pebbles) occurred from higher latitudes to the equatorial region during the formation of the equatorial ridge of Ryugu. These small particles bury themselves and some large blocks, so the block size distribution in the local area may depend on the amount of migrated small particles. For instance, in the case of Bennu, a recent study by Barnouin et al. (2022) shows that the amount of migrated material on the surface depends on the localized topography. Thus, there are several possibilities for explaining the relation between the block sizes and the power-indices of the size distribution. After all, differences in terrain properties and/or preservation can result in a spread in the power-index.

Fig. 13 shows the correlation between the mean c/a ratios of blocks and the power-indices of the size distributions. Regions with mean c/a ratios less than 0.42 were only found at altitudes higher than 450 m and here shapes are likely to be affected by migrated material. Except for these data, the shapes of small blocks are roughly constant, and independent of the power-indices. This implies that further comminution by repeated impacts (cratering and/or catastrophic disruptions) is unlikely to affect block shapes. In other words, on a rubble-pile body, fragment shapes seem to remain similar, independent of whether they resulted from local cratering and/or catastrophic disruptions.

This is in contrast to the Moon and Mars, where abrasion during movement for long periods and over long distances (which is much longer than that of asteroid materials) can affect fragment shapes, turning particles more spherical. On the Moon for example, Katagiri et al. (2014) have examined the three-dimensional microstructure of 74 lunar regolith particles from Apollo 16 with sizes from 105 to 205 μm using synchrotron radiation (SR)-based microtomography at SPring-8. The results show mean b/a and c/a axial ratios of 0.79 and 0.59, respectively. As a general rule, particles on Mars are much more rounded because of the dominance of aeolian (and often previously fluvial) erosion. The Curiosity rover for example found rounded pebbles with $b/$

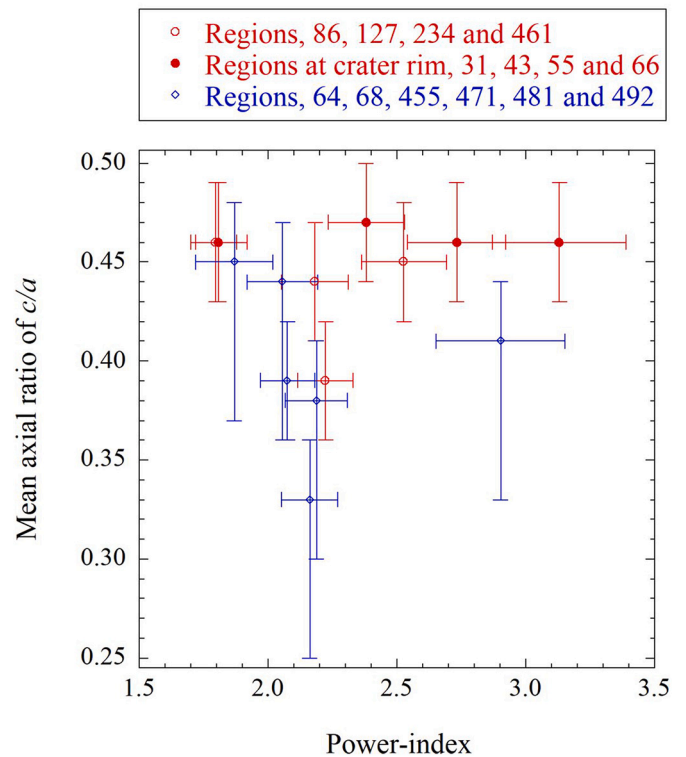


Fig. 13. Diagram of the mean c/a ratios vs. the power-indices of the cumulative block size distributions of the small blocks in several local regions. Region numbers of the second touch-down sequence and other local regions in this study are shown in red and blue, respectively. The data lists are given in Table 2. (For interpretation of the references to colour in this figure legend, the reader is referred to the web version of this article.)

a values close to 0.8, and Szabo et al. (2015) highlight how abrasion by inter-particle collisions played a key role in shaping these particles. In this sense, small blocks on Ryugu show no evidence of abrasion.

Put together, all the above could mean that, on Ryugu, the dominant shape-determining process is not thermal fatigue but impact fragmentation. Given that evidence of thermal fatigue is widespread on Bennu, it could be interesting to explore the conditions that favour one process over another.

5. Conclusions

We have investigated the three-axial ratios of \sim 4100 small blocks with diameters of 5.0 cm to 7.6 m in Ryugu's equatorial region using eight close-up images of narrower localities taken at altitudes below 500 m at $<5.4 \text{ cm/pixel}$, resolution, obtained immediately before the second touch-down of the Hayabusa2 spacecraft. The power-indices of the cumulative block size distributions show some scatter, ranging from -1.80 ± 0.08 to -3.13 ± 0.26 , which may be due to differences in terrain properties and/or preservation. The shape distributions of blocks indicate that the mean b/a ratios of blocks are similar, approximately 0.7, resembling the shapes of laboratory impact fragments (Fujiwara et al., 1978; Capaccioni et al., 1984, 1986; Michikami et al., 2016, 2018). The mean c/a ratios of blocks less than 1 m in diameter are similar, approximately 0.46, which is also in line with laboratory impact fragments. However, at 0.39 or less, the mean c/a ratio of blocks several meters in diameter seems to be slightly smaller, meaning that the heights of these blocks are relatively small compared with their diameters. A plausible explanation is that some of the larger blocks in the equatorial region are partly or mostly buried in a substrate of fine-grained material and/or small blocks less than 1 m, as pointed out by Michikami et al. (2019) and Tanabe et al. (2021). As a result of partial burial, the actual

mean c/a ratios of blocks in this size range can be expected to be larger than the apparent, measured values. The fact that the three-axial shape distribution of small blocks in Ryugu's equatorial region is similar to laboratory impact fragments suggests most small blocks are impact fragments originating from a catastrophic disruption, possibly comminuted by a later impact.

The results of this first quantitative investigation of the three-axial shape distribution of blocks on a real asteroid will be useful for understanding the formation and migration of blocks and for ensuring a safe touchdown of the future landing missions on asteroids.

Declaration of Competing Interest

None.

Appendix A. Investigation of the difference between real height of the fragment and its height estimated from the shadow

In this study, the heights of small blocks on Ryugu are estimated from their shadow lengths. However, because the height is the edge height of the block casting the shadow, it is possible that the height is underestimated when the block's top surface is convex or has pointy features. Therefore, using the data of real impact fragments as a proxy, we try to investigate the difference between real height of the fragment and the height estimated from the shadow length. Note that this is only the first step towards a better understanding of the difference, in the future a more quantitative investigation might be needed.

We use fragments from laboratory impact experiments into basalts (Michikami et al., 2016) as analogues. Upon cursory investigation, there are few fragments with a pointy feature the middle of the surface when the fragment was positioned with its c axis perpendicular to the floor. Michikami et al. (2018) adopted the archived small particles of Michikami et al. (2016) and investigated two thousand fine fragments smaller than $120\ \mu\text{m}$ by synchrotron radiation-based microtomography at Spring-8 at a spatial resolution of $1.74\ \mu\text{m}/\text{voxel}$. The three dimensional shape models of these fine fragments are useful for examining the height as estimated from the length of shadow. Using the data of Michikami et al. (2016, 2018), the following three points are investigated.

(i) Influence of shadow direction on estimated height for a fine fragment

Even when a single fragment is observed, its edges have different heights, i.e. the height estimation depends on the shadow direction. Firstly, we selected an arbitrary fine fragment with the three axial lengths, $718 \times 488 \times 250\ \mu\text{m}$ in shot s2131 measured by microtomography (Michikami et al., 2018). We produce sixteen virtual shadows of the fine fragment, i.e. two light incidences of $i = 15^\circ$ and 30° (Fig. A1(a)) and eight incident azimuth angles of the light by every 45° (Fig. A1(b)).

Fig. A1(c) indicates the relationship between the real height (measured by microtomography) and the heights estimated from the virtual shadow lengths. The heights estimated from the shadows are smaller than the real height. The estimated heights somewhat differ depending on the incident azimuth angles of the light. The lowest estimated heights at the incident azimuth angle of $\theta = 90^\circ$ mean that the fragment surface has a gentle slope. The estimated heights at a light incidence of $i = 30^\circ$ are larger than at $i = 15^\circ$, suggesting that the shadow data at incidence angles greater than 30° are more reliable to estimate the heights of the blocks. The average shadow-estimated versus real heights at an incidence angle of $i = 15^\circ$ and 30° are 0.73 ± 0.10 and 0.86 ± 0.13 , respectively.

(ii) Heights estimated at arbitrary light incidence angles for 31 fine fragments

On a real asteroid surface, the directions of the longest dimension of the blocks would be random and thus their light would have various incident azimuth angles. To simulate this, we estimate the heights of 31 fine fragments (sphere-equivalent diameter, $120\ \mu\text{m}$ to $750\ \mu\text{m}$) from shot s2131 analyzed by Michikami et al. (2018) by lighting them from arbitrary incidence azimuth angles. These fragments have mean b/a and c/a ratios of 0.73 and 0.44, respectively.

Fig. A2 shows the relationship between the heights estimated from the virtual shadows produced by lighting from arbitrary azimuth incidence angles and the real heights of these 31 fragments. The light incidence was kept at $i = 30^\circ$. The results indicate that the heights of most fragments can be estimated, with estimates ranging from 0.8 to 1.1 compared to the real heights. The reason for the overestimated heights (> 1) is that a part of the fragment is tilted upwards, which is often observed when the fragments are put on the floor. Underestimated heights (< 0.8) mean that these fragments have a pointy feature on one surface and as the result their edge heights are relatively small. The average ratio of estimated vs real heights at incidence angle $i = 30^\circ$ is 0.88 ± 0.16 .

(iii) Heights estimated from the shadows for 15 fragments on a model of an asteroid surface

The results of (i) and (ii) above are derived from virtual shadow lengths. However, because a real asteroid surface is covered with blocks and particles of various sizes, the shadow lengths of blocks may depend on the topographic features on the surface. To investigate this influence, using the fragments produced by shot s2131 in Michikami et al. (2016) we created a model of an asteroid surface consisting of small particles with diameters of $\sim 2\ \text{mm}$ and deposited 15 fragments with diameter of $\sim 10\ \text{mm}$ gently, with their c axes oriented perpendicular to the surface (Fig. A3(top)). We exposed this surface to sunlight with incidence angle $i = 32.2^\circ$. After taking an image, the apparent three lengths of 15 fragments are measured using SAOImage DS9. The apparent lengths of a and b are obtained as the longest and shortest axes of ellipses, respectively. Taking account for the position of the Sun and the camera, the heights (h) of small fragments are determined by $h = \frac{l}{\tan i + \tan e}$, where l , i and e are the shadow length, the solar incidence angle, and the emission angle, respectively. In the experiment, because h of all fragments are smaller than a and b , h is equal to c . After analyzing the

Acknowledgements

The authors would like to thank all members of Hayabusa2 mission team for their support of the data acquisition of Ryugu. We thank Dr. S. Hasegawa and Dr. H. Naruse for useful discussions. We also thank two anonymous referees for their careful review of the manuscript and their constructive comments. The research was supported by the Japan Society for the Promotion of Science (JSPS) KAKENHI (Grant Number 20K04048 for TM, 20H00194 for SS and 15H02146 for AT) and Core-to-Core program "International Network of Planetary Sciences." AT was also supported by Chinese Academy of Sciences President's International Fellowship Initiative, Grant No.2019VCA0004. This study was partly supported by the Hypervelocity Impact Facility, ISAS, JAXA.

image, the three lengths of the 15 fragments are accurately measured with digital calipers.

Fig. A3 (bottom) show the relationship between the three lengths estimated from the image and those measured with calipers. The straight line connects the points where the lengths estimated from the image and those measured with calipers are the identical. In the cases of a and b , estimated lengths are similar to measured lengths. The mean ratios of estimated to measured lengths are 1.03 ± 0.07 for the a axis and 1.00 ± 0.07 for b . In the case of c , the estimated lengths are slightly smaller than measured lengths. However, the differences are only minor and the mean ratios of estimated versus measured heights are very close to one, namely 0.96 ± 0.12 .

From the results of (i) (ii) and (iii), we conclude that each block height on Ryugu can be derived from shadow lengths within a precision of at least 20% and mean block heights on Ryugu can be estimated within a precision of at least 10%.

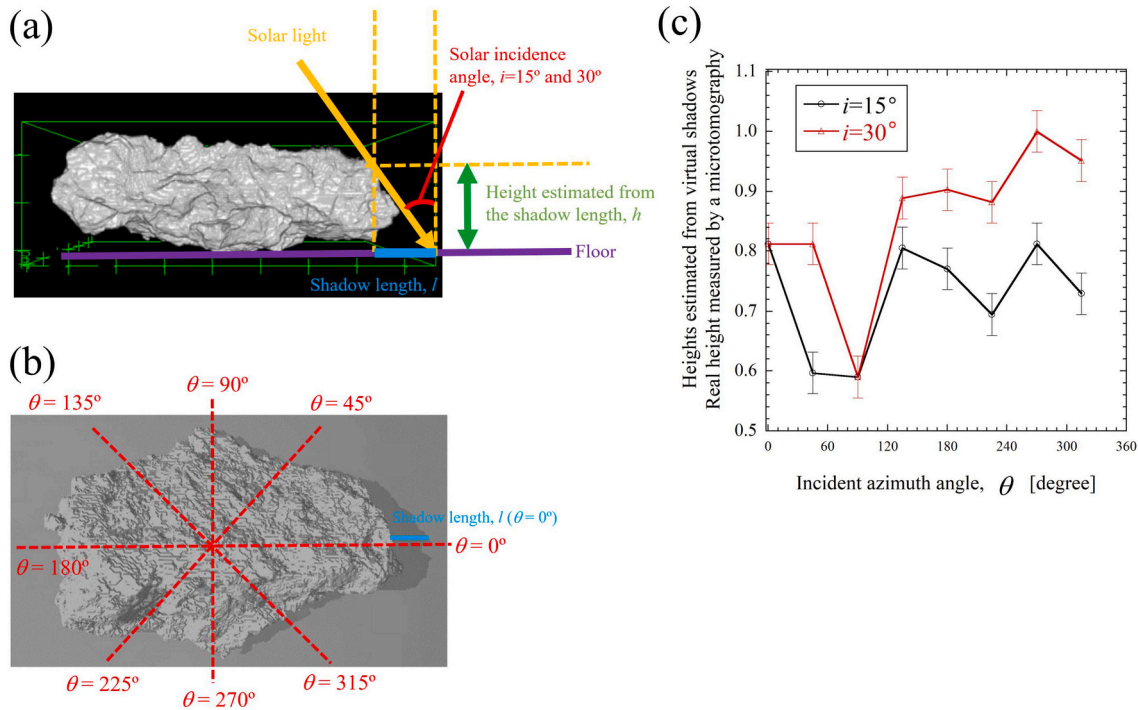


Fig. A1. (a) A shape model of a fine fragment with axial lengths $718 \times 488 \times 250 \mu\text{m}$ from shot s2131 measured by microtomography (Michikami et al., 2018). The illustration shows the shadow at an azimuth angle of $\theta = 0^\circ$. (b) Shows the same particle shape model, whose lateral and longitudinal directions in the illustration are the a and b axial directions, respectively. (c) Heights estimated from virtual shadows vs. azimuth angles of the small particle illustrated by (a) and (b). The vertical axis shows the ratios of shadow-estimated to real heights as measured by microtomography. The horizontal axis indicates the azimuth angles, θ , of the light. Black and red points indicate light incidence angles of $i = 15^\circ$ and 30° , respectively. (For interpretation of the references to colour in this figure legend, the reader is referred to the web version of this article.)

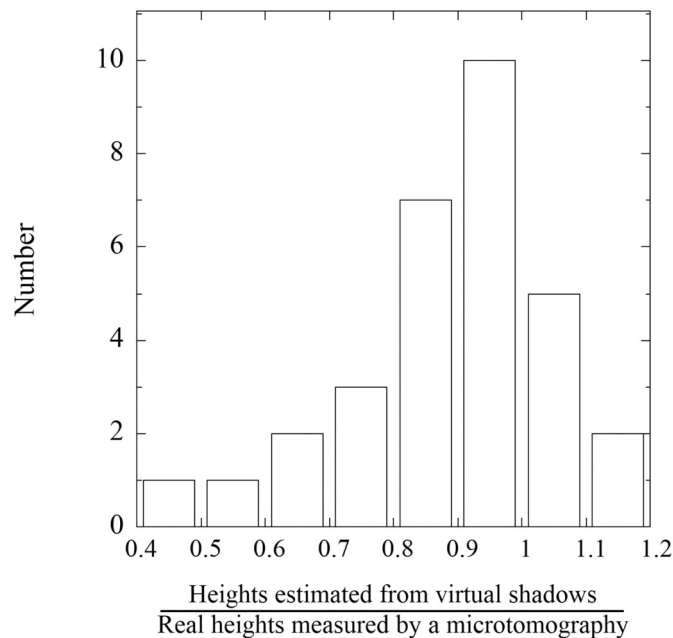


Fig. A2. Histogram of ratios of estimated to real heights for 31 fragments at a light incidence of $i = 30^\circ$, with arbitrary azimuth angles of illumination.

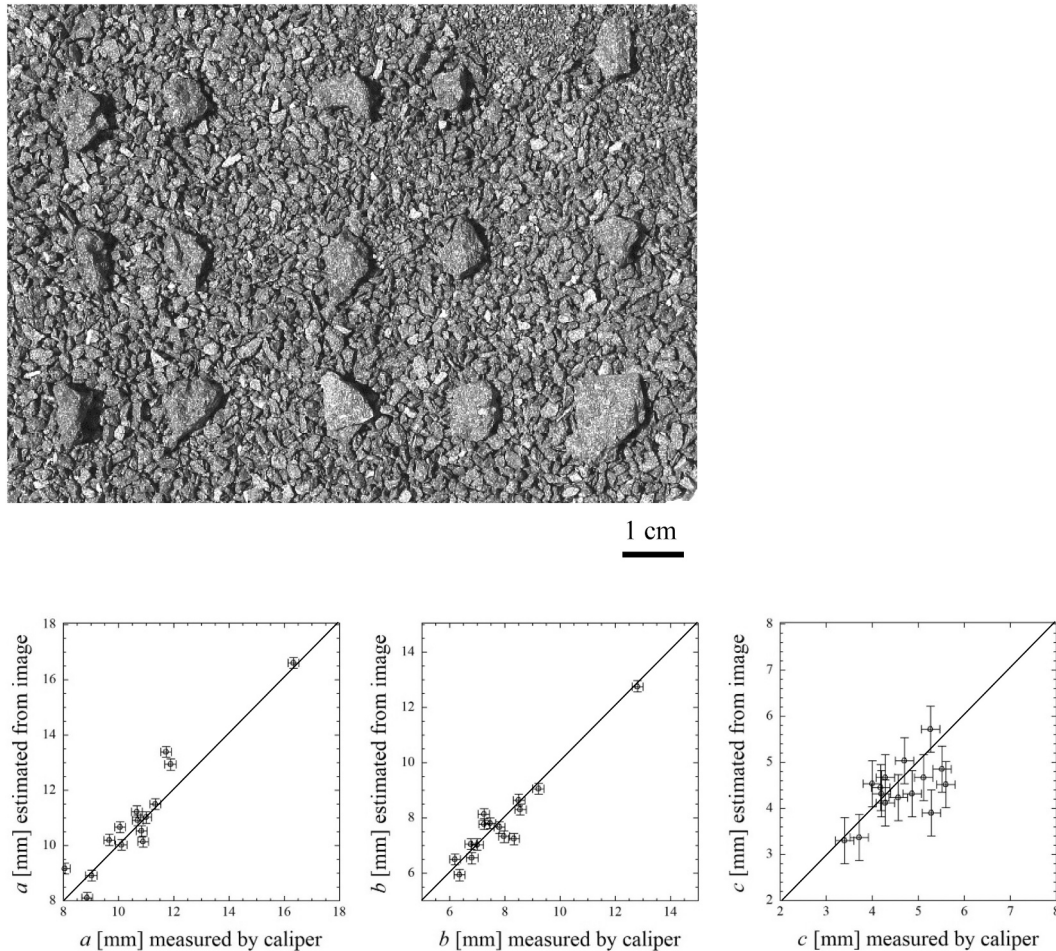


Fig. A3. Top: image of 15 basalt fragments with diameters of ~ 10 mm selected from shot s2131 in Michikami et al. (2016). It simulates a relatively rough region of an asteroid surface. Bottom: axial lengths a , b , and c of the 15 fragments measured by calipers vs. lengths estimated from the image.

References

- Arakawa, M., Saiki, T., Wada, K., et al., 2020. An artificial impact on the asteroid (162173) Ryugu formed a crater in the gravity-dominated regime. *Science* 368, 67–71.
- Barnouin, O.S., Daly, M.G., Seabrook, J.A., et al., 2022. The formation of terraces on asteroid (101955) Benu. *J. Geophys. Res. Planet.* In press.
- Cambioni, S., Delbo, M., Poggiali, G., et al., 2021. Fine-regolith production on asteroids controlled by rock porosity. *Nature* 598, 49–52.
- Capaccioni, F., Cerroni, P., Coradini, M., et al., 1984. Shapes of asteroids compared with fragments from hypervelocity impact experiments. *Nature* 308, 832–834.
- Capaccioni, F., Cerroni, P., Coradini, M., et al., 1986. Asteroidal catastrophic collisions simulated by hypervelocity impact experiments. *Icarus* 66, 487–514.
- Cho, Y., Morota, T., Kanamaru, M., et al., 2021. Geologic history and crater morphology of asteroid (162173) Ryugu. *J. Geophys. Res. Planet.* 126. <https://doi.org/10.1029/2020JE006572> e2020JE006572.
- Clauset, A., Shalizi, C.R., Newman, M.E.J., 2009. Power-law distributions in empirical data. *SIAM Rev.* 51, 661–703.
- Delbo, M., Libourel, G., Wilkerson, J., et al., 2014. Thermal fatigue as the origin of regolith on small asteroids. *Nature* 508, 233–236. <https://doi.org/10.1038/nature13153>.
- Dombard, A.J., Barnouin, O.S., Prockter, L.M., Thomas, P.C., 2010. Boulders and ponds on the Asteroid 433 Eros. *Icarus* 210, 713–721.
- Durda, D., Bagatin, A., Aleman, R.A., et al., 2015. The shapes of fragments from catastrophic disruption events: effects of target shape and impact speed. *Planet. Space Sci.* 107, 77–83.
- Fujiwara, A., Kamimoto, G., Tsukamoto, A., 1978. Expected shape distribution of asteroids obtained from laboratory impact experiments. *Nature* 272, 602–603.
- Gaddis, L.R., McEwen, A.S., Becker, T.L., 1995. Compositional variations on the Moon: recalibration of Galileo solid-state imaging data for the Orientale region and farside. *J. Geophys. Res. Planet.* 100, 26345–26355.
- Grott, M., Knollenberg, J., Hamm, M., et al., 2019. Low thermal conductivity boulder with high porosity identified on C-type asteroid (162173) Ryugu. *Nat. Astron.* 3, 971–976. <https://doi.org/10.1038/s41550-019-0832-x>.
- Hartmann, W.K., 1969. Terrestrial, lunar, and interplanetary rock fragmentation. *Icarus* 10, 201–213.
- Honda, R., Arakawa, M., Shimaki, Y., et al., 2021. Resurfacing processes on asteroid (162173) Ryugu caused by an artificial impact of hayabusa2's small carry-on impactor. *Icarus* 366, 114530.
- Ishiguro, M., Nakamura, R., Tholen, D.J., et al., 2010. The Hayabusa spacecraft asteroid multi-band imaging camera (AMICA). *Icarus* 207, 714–731.
- Jawin, E.R., Walsh, K.J., Barnouin, O.S., et al., 2020. Global patterns of recent mass movement on asteroid (101955) Benu. *J. Geophys. Res. Planet.* 125. <https://doi.org/10.1029/2020JE006475> e2020JE006475.
- Katagiri, J., Matsushima, T., Yamada, Y., et al., 2014. Investigation of 3D grain shape characteristics of lunar soil retrieved in Apollo 16 using image-based discrete-element modeling. *J. Aerosp. Eng.* 28 (4), 04014092. [https://doi.org/10.1061/\(asce\)as.1943-5525.0000421](https://doi.org/10.1061/(asce)as.1943-5525.0000421).
- Kikuchi, S., Watanabe, S., Saiki, T., et al., 2020. Hayabusa2 landing site selection: surface topography of Ryugu and touchdown safety. *Space Sci. Rev.* 216, 116.
- Lauretta, D.S., DellaGiustina, D.N., Bennett, C.A., et al., 2019. The unexpected surface of asteroid (101955) Benu. *Nature* 568, 55–60. <https://doi.org/10.1038/s41586-019-1033-6>.
- Lucy, L.B., 1974. An iterative technique for the rectification of observed distributions. *Astron. J.* 79, 745–754.
- Michikami, T., Hagermann, A., 2021. Boulder sizes and shapes on asteroids: a comparative study of Eros, Itokawa and Ryugu. *Icarus* 357, 114282.
- Michikami, T., Nakamura, A.M., Hirata, N., et al., 2008. Size-frequency statistics of boulders on global surface of asteroid 25143 Itokawa. *Earth Planet Space* 60, 13–20.
- Michikami, T., Nakamura, A.M., Hirata, N., 2010. The shape distribution of boulders on asteroid 25143 Itokawa: comparison with fragments from impact experiments. *Icarus* 207, 277–284.
- Michikami, T., Hagermann, A., Kadokawa, T., et al., 2016. Fragment shapes in impact experiments ranging from cratering to catastrophic disruption. *Icarus* 264, 316–330.
- Michikami, T., Kadokawa, T., Tsuchiyama, A., et al., 2018. Influence of petrographic textures on the shapes of impact experiment fine fragments measuring several tens of microns: comparison with Itokawa regolith particles. *Icarus* 302, 109–125.
- Michikami, T., Honda, C., Miyamoto, H., et al., 2019. Boulder size and shape distributions on asteroid Ryugu. *Icarus* 331, 179–191.

- Molaro, J.L., Hergenrother, C.W., Chesley, S.R., et al., 2020. Thermal fatigue as a driving mechanism for activity on asteroid Bennu. *J. Geophys. Res. Planet.* 125. <https://doi.org/10.1029/2019JE006325> e2019JE006325.
- Okada, T., Fukuhara, T., Tanaka, S., et al., 2020. Highly porous nature of a primitive asteroid revealed by thermal imaging. *Nature* 579, 518–522. <https://doi.org/10.1038/s41586-020-2102-6>.
- Richardson, W.H., 1972. Bayesian-based iterative method of image restoration. *J. Opt. Soc. Am.* 62, 55–59.
- Sugita, S., Honda, R., Morota, T., et al., 2019. The geomorphology, color, and thermal properties of Ryugu: implications for parent-body processes. *Science* 364. <https://doi.org/10.1126/science.aaw0422>.
- Szabo, T., Domokos, G., Grotzinger, J.P., et al., 2015. Reconstructing the transport history of pebbles on Mars. *Nat. Commun.* 6, 8366. <https://doi.org/10.1038/ncomms9366>.
- Tanabe, N., Cho, Y., Tatsumi, E., et al., 2021. Development of image texture analysis technique for boulder distribution measurements: applications to asteroids Ryugu and Itokawa. *Planet. Space Sci.* 204, 105249.
- Tancredi, G., Roland, S., Bruzzone, S., 2015. Distribution of boulders and the gravity potential on asteroid Itokawa. *Icarus* 247, 279–290.
- Thomas, P.C., Veveřka, J., Robinson, M.S., Murchie, S., 2001. Shoemaker crater as the source of most ejecta blocks on the asteroid 433 Eros. *Nature* 413, 394–396.
- Tsuchiyama, A., Uesugi, M., Uesugi, K., et al., 2014. Three-dimensional microstructure of samples recovered from asteroid 25143 Itokawa: comparison with LL5 and LL6 chondrite particles. *Meteorit. Planet. Sci.* 49, 172–187.
- Veveřka, J., Farquhar, B., Robinson, M., et al., 2001. The landing of the NEAR-Shoemaker spacecraft on asteroid 433 Eros. *Nature* 413, 390–393.
- Walsh, K.J., Jawin, E.R., Ballouz, R.-L., et al., 2019. Craters, boulders and regolith of (101955) Bennu indicative of an old and dynamic surface. *Nat. Geosci.* 12, 242–246. <https://doi.org/10.1038/s41561-019-0326-6>.
- Watanabe, S., Hirabayashi, M., Hirata, N., et al., 2019. Hayabusa2 arrives at the carbonaceous asteroid 162173 Ryugu—a spinning top-shaped rubble pile. *Science* 364, 268–272. <https://doi.org/10.1126/science.aav8032>.
- Wentworth, C.K., 1922. A scale of grade and class terms for clastic sediments. *J. Geol.* 30, 377–392.
- Yano, H., Kubota, T., Miyamoto, H., et al., 2006. Touchdown of the Hayabusa Spacecraft at the Muses Sea on Itokawa. *Science* 312, 1350–1353.